Letters in Applied NanoBioScience
Open-Access Journal (ISSN: 2284-6808)

Article

Volume 15, **Issue 2**, **2026**, **74**
https://doi.org/10.33263/LIANBS152.074

Investigation of Structural, Magnetic, and Electrochemical Properties of Samarium Doped Strontium Hexaferrites Prepared via Auto-Combustion Method

Ankyanaik Thippeswamy [1], **Prabhakar Chavan** [2], **Ganganaik Krishnamurthy** [3,*]

[1] Department of PG Studies in Industrial Chemistry, Government Arts and Science College, Karwar, Karnataka, India
[2] Department of Studies and Research in Chemistry, Sahyadri Science College, Kuvempu University, Shivamogga, Karnataka, India
[3] Department of PG Studies and Research in Industrial Chemistry, Sahyadri Science College, Kuvempu University, Shivamogga, Karnataka, India
* Correspondence: gkmnaiksahyadri@gmail.com;

Received: 11.03.2025; Accepted: 24.02.2026; Published: 30.06.2026

Abstract: Samarium-doped strontium hexaferrites (SmSrHF's) of the formulae $SrFe_{12-x}Sm_xO_{19}$ (x=0.00, 0.01, 0.05, and 0.09) were synthesized by the auto-combustion method using urea as a fuel. The microstructural properties of SmSrHF's were investigated by X-ray diffraction (XRD) and field emission scanning electron microscopy (FE-SEM). The spectral data indicated that the synthesized nanomaterials have a crystalline size range from 30 to 35 nm and possess a pure hexagonal crystal structure. Elements present in the compounds were verified by energy-dispersive X-ray spectroscopy (EDX), and thermal stability was determined by thermogravimetric analysis (TGA). The vibrating sample magnetometer (VSM) was used to study the hysteresis loop, which showed that the saturation magnetization(Ms) is from 36 to 40 emu/g and the remanence (Mr) increases from 20 to 22 emu/g, as the substitution of samarium ions increases. The modified electrode was prepared by using synthesized nanomaterials to study the electrochemical behavior. Two simple techniques, such as cyclic voltammetry (CV) and differential pulse voltammetry (DPV), connected with a modified electrode, gave a long linear range. The result showed a range from 20 to 100 $\mu molL^{-1}$, a sensitivity of 0.0113 $\mu A \mu M^{-1} cm^{-2}$, and LOD is 6.667 μML^{-1}. The modified electrode was also employed to detect the presence of folic acid, a biologically important molecule in the sample.

Keywords: hexaferrites; auto-combustion; cyclic voltametry; TGA; Folic acid; DPV; vibrating sample magnetometer; peak current.

1. Introduction

In modern times, strontium ferrite oxides play an important role in various sectors. They are used in multiple technologies in magnetic memories [1], chemical sensing [2], computer technologies [3], telecommunication [4], electrical conductivity [5], generator rotors in electric vehicles [6], energy [7], magnetization [8], electrochemical energy storage [9], and transformers [10]. Efficient heat dissipation in electronic devices is hindered by high power consumption and heat flux, which are essential for 5G technology [11], bioimaging, and biosensing [12]. In view of their importance, a number of nanomaterials have been synthesized and their properties studied. The literature review shows that strontium ferrites are the best hard magnetic materials suitable for high-frequency applications and thermal-stability composites [13]. Owing to its high magnetic coercivity, high electrical resistivity, low conductive loss, fairly high mechanical hardness, and chemical stability [14]. Strontium ferrites and mixed ferrite nanoparticles are widely investigated, and their properties are tuned by doping transition metals. Presence of a very small amount of elements with large ionic radii in the spinel lattice can greatly improve the structural, electric, and magnetic properties of M-type strontium hexaferrites (M-SrHF’s) [15]. Research in the recent decade indicated that the rare-earth element samarium (Sm) is widely used as a dopant to promote numerous heterogeneous catalytic reactions. The synthesized Sm doped MnO_xTiO_2 catalyst was used for the selective catalytic reduction of NO_x with NH_3. The samarium in the catalyst can enhance the surface area and thus increase the surface active sites, which results in NO_x conversion [16]. The magnetic properties of rare-earth-element-substituted ferrites provide insight into cations that can influence crystal and surface structural properties [17,18]. The optical properties of nanocomposites containing rare-earth elements are critical due to the presence of multiple unpaired 4f electrons and their ionic radii [19]. Therefore, selecting a new dopant type and the amount of dopant to achieve the specific target are very important.

Folic acid is an essential component of prenatal vitamins that occurs in many cereals and pastas. Folic acid is very important for DNA synthesis and repair. It has excellent curative properties and helps treat low levels of vitamin B_9 in the human body, which is important for making red blood cells and maintaining brain health. Deficiency of folic acid in animals causes various health issues, including anemia, poor growth, and reproductive problems, and in humans, its deficiency leads to several health issues, including megaloblastic anemia, which causes fatigue and weakness. There are recent reports on using ionic liquids to design highly sensitive electrochemical sensors [20]. Its deficiency also causes neural tube defects during early pregnancy. Therefore, the detection of folic acid in the biological system is very important [21].

The effect of Ce^{3+}, Gd^{3+}, and Er^{3+} substitution in strontium hexaferrite, their structure, magnetic properties, and catalytic properties have been studied in our laboratory [22,16,17]. In continuation, in the present investigation, Sm^{3+} doped strontium hexaferrite has been prepared by an auto-combustion technique using low-cost and easily available urea as a fuel. The present synthetic method has numerous benefits over the other conventional methods. In addition, these Sm^{3+} doped strontium hexaferrites enable the detection of biologically important molecules like folic acid. The electrochemical parameters, including scan rate at different concentrations, sensitivity, linear range, limit of detection (LOD), and differential pulse voltammetry parameters, were also studied.

2. Materials and Methods

All chemicals are analytical grade, Samarium nitrate hexahydrate, $Sm(NO_3)_3.6H_2O$, Ferric nitrate nanohydrates, $Fe(NO_3)_3.9H_2O$, Strontium nitrate, $Sr(NO_3)$, and urea, (CH_4N_2O), and distilled water, which were used as such, the solvents used after distillation.

2.1. Syntheses of $SrFe_{12-x}Sm_xO_{19}$ (x=0.00, 0.01, 0.05, and 0.09) nanoparticles.

Synthesis of samarium-doped strontium hexaferrite by the auto-combustion method. The precursors and organic fuels used were of analytical grade. The metal precursors used were samarium nitrate hexahydrate, $Sm(NO_3)_36H_2O$, iron (III) nitrate nanohydrates, $Fe(NO_3)_39H_2O$, strontium nitrate, $Sr(NO_3)_2$ and urea, (CH_4N_2O) were taken in aqueous solution in a cylindrical petri dish placed into a furnace to attain a temperature of 500 °C for five minutes. The reaction mixture releases a large amount of N_2O and CO_2 gas and heat [23]. The sintered powders were ground in a mortar and pestle. The powder was mixed with a binder, polyvinyl pyrolidone $(C_6H_9NO)_n$. The pellets are sintered in a furnace at 1200 °C for 4h and then gradually cooled to room temperature. The synthesized nanoparticles were characterized using FTIR, XRD, VSM, DSC/TG, and their electrochemical behavior was evaluated.

2.2. Electrochemical analysis: Apparatus and Procedure.

Folic acid obtained from Sigma-Aldrich was dissolved in ethanol to prepare 10 mM standard stock solutions and stored in the dark. $SrFe_{12-x}Sm_xO_{19}$ (x= 0.09) was dissolved in double-distilled water to form 5 mM solutions. Phosphate buffer solution (PBS) was prepared by the standard method. All experiments were performed at room temperature.

The electrochemical experiments were carried out using a Model CHI-660C electrochemical work station. All experiments were carried out in a conventional three-electrode system. The electrode system contained a working carbon paste electrode with a homemade cavity of 3 mm in diameter, a platinum wire as the counter electrode, and a saturated calomel electrode as the reference electrode.

3. Results and Discussion

3.1. Powder X-ray diffraction.

The X-ray pattern of the synthesized $SrFe_{12-x}Sm_xO_{19}$ (x=0.00, 0.01, 0.05, and 0.09) nanoferrites is shown in Figure 1. The planes (110), (114), (200), and (203) compared with the JCPDS card number 24-1207, which matches the hexagonal phase. XRD studies give the lattice parameter, which gradually increases from 0.510 to 0.572 cm^{-1}, and the increase in Sm^{3+} ion concentration, which increases the lattice parameter due to the substitution of larger Sr^{2+} (0.112 nm) with smaller Sm^{3+} ions (0.1098 nm) [24].

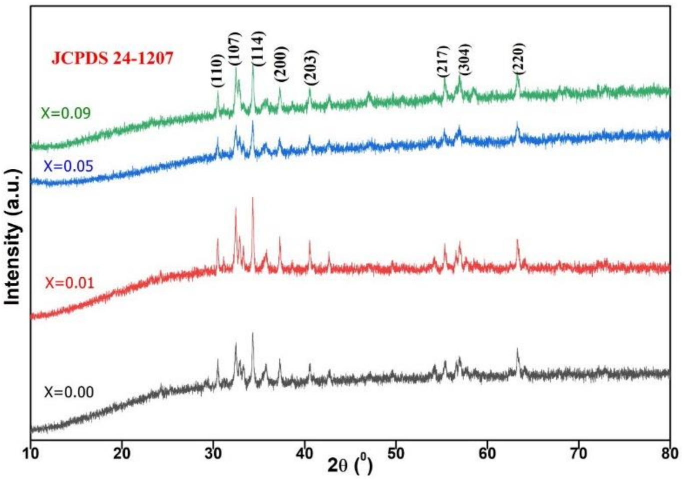

Figure 1. XRD pattern of $SrFe_{12-x}Sm_xO_{19}$ (x=0.00, 0.01, 0.05, and 0.09).

The unit cell of the hexagonal system is calculated by the relation V cell = 0.866 a^2c, where a and c are the lattice parameters sustained for the hexagonal system. Using the Debye-Scherrer equation to determine the average crystalline size of the synthesized nanoparticle. From the XRD profile, the average size of the nanoferrite crystallites was determined using the Debye-Scherrer equation, and the results are presented in Table 1. The values of the c/a ratio were reported in Table 1, and the hypothetical X-ray thickness (dx) of each sample was determined.

Table 1. Crystallite size (D), lattice constant (a and c), cell volume (V), and X-ray density (qx-ray) of $SrFe_{12-x}Sm_xO_{19}$ (x=0.00, 0.01, 0.05, and 0.09) nanoferrites.

Composition	**Crystallite size (D) /nm**	**Lattice constant (a)/Å**	**Lattice constant (c)/ Å**	**(c)/(a) Å**	**Cell volume (V)/Å³**	**X-ray density (qx-ray)/g cm⁻³**
$SrFe_{12}O_{19}$	31.02	5.87	22.3	3.913	691.38	0.510
$SrSm_{0.01}Fe_{11.99}O_{19}$	30.63	5.88	23.0	3.916	691.38	0.580
$SrSm_{0.05}Fe_{11.95}O_{19}$	30.39	5.88	23.0	3.916	691.38	0.576
$SrSm_{0.09}Fe_{11.91}O_{19}$	30.29	5.88	23.0	3.916	691.38	0.572

X-ray thickness is in the range 0.510 to 0.572 cm^{-1}. The decrease in the X-ray thickness was more because of the doping of the Sm^{3+} ion with a larger molecular weight (104.116 amu) and with the ion volume (0.1034 nm) when compared to the Sr^{2+} ion with a smaller molecular weight (87.62 amu) and the largest ion radius (0.112 nm).

3.2. Fourier transform infrared measurements.

FTIR spectra of synthesized $SrFe_{12-x}Sm_xO_{19}$ (x=0.00, 0.01, 0.05, and 0.09) are shown in Figure 2. Three peaks are expected in the region 450-480 cm^{-1}, 500-550 cm^{-1} and 443 cm^{-1}. The functional group of NO_3^- that has been completely decomposed and thus in the synthesized sample, the vibrational bands of this group did not appear [25]. The two bands at 500 and 580cm^{-1} are observed for the hexagonal lattice and are the direct result of metal-oxygen stretching vibrations [26]. Due to various ionic vibrations in the crystal lattice of a hexagonal structure, the metal ion-oxygen bond formation in the domains of octahedral and tetrahedral was obtained (2B). A small change in the position of the IR peak shows that the replacement of Sr^{2+} by Sm^{3+} occurs without changing the crystal structure of the composition. In this reaction, the OH group is absent because the band around 3500 cm^{-1} was not observed.

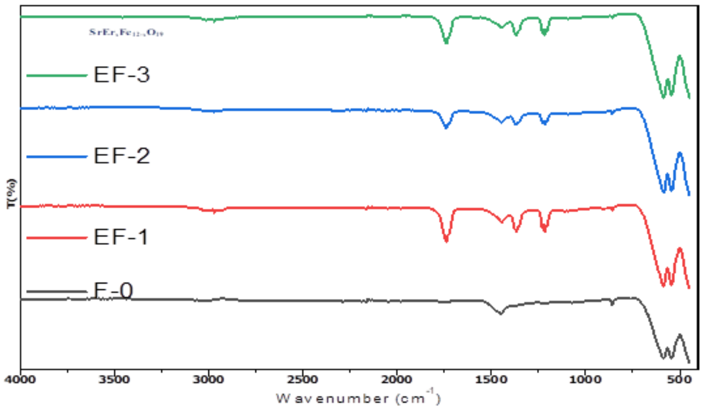

Figure 2. FTIR spectra of sintered powder of $SrFe_{12-x}Sm_xO_{19}$ (x=0.00, 0.01, 0.05, and 0.09) nanoferrites.

3.3. Morphological studies.

The prepared $SrFe_{12-x}Sm_xO_{19}$ (x=0.00, 0.01, 0.05, and 0.09) was used to predict the morphology and microstructure, as shown in supplementary Figure S1. The SEM image clearly showed hexagonal platelets and agglomerates with a regular shape at higher concentration, accompanied by a decrease in particle size. This phenomenon is an indication of the deposition of Sm^{3+}. As shown in Table 1, the grain size was found in the range 1.42-2.43 µm for M-type hexaferrites, and the larger grain size can be accomplished by high calcination temperatures. Therefore, saturation magnetization is high in materials that influence the enhancement of permeability. It was observed that the grain size of the sample is bigger than that of the samarium (Sm^{3+}) substituted hexaferrites.

The elemental mapping by EDX for $SrFe_{12-x}Sm_xO_{19}$ is shown in Supplementary Figure S2. The EDX spectra showed the presence of Sr, Fe, Sm, and O elements. The results of EDX measurements show that the appearance of their corresponding peaks without any other characteristic peaks suggests that the prepared samples are not contaminated during the synthetic process.

3.4. DSC –TGA studies.

A thermogravimetric experiment was performed using 10 mg at a heating rate of 5° /min in static air. The results obtained in TGA indicate three stages of weight loss. The degradation graph shows a weight loss curve ranging from 70 to 115 °C due to the loss of lattice water molecules. The second step, an exothermic reaction occurs, 264 °C due to decoposion of organic molecules (PVP) and produces a broad degradation curve up to 600 °C for the formation of ferrite nanoparticles [27-29].

3.5. Magnetic measurements.

The measurements of magnetization were applied using a magnetic field of 8 Oe with a maximum field of 70 Oe at room temperature using a vibrating sample Magnetometer (VSM). Figure 3 shows the MH-loops for M-type hexagonal ferrites $SrFe_{12-x}Sm_xO_{19}$ (x=0.00, 0.01, 0.05, and 0.09). The magnetic properties like retentivity (Mr), saturation magnetization (Ms), squareness ratio (Mr/Ms) and coercivity (Hc), are extracted from hysteresis curves and presented as a function of Sm doping [30,31] as shown in Figure 3.

The electronic configuration of the substituted cations (or doped material) affects the magnetic properties of substituted hexagonal ferrites. Electronegativity of substituted samarium (Sm^{3+}) is 1.17. Each Fe^{3+} ion has five unpaired electrons, and in the hexagonal ferrites, five different sub-lattices are occupied by a total of 12 Fe^{3+}, in which the crystal structure contains three octahedral sites (12k, 2a, and 4f2), one tetrahedral site (4f1), and one trigonal bipyramidal site (2b). Among the 12 Fe^{3+} ions, four exhibit spins aligned in the downward direction, with two Fe^{3+} ions occupying the 4f1 tetrahedral site and two Fe^{3+} ions occupying the 4f2 octahedral site. The remaining eight Fe^{3+} ions, located at the 12k, 2a, and 2b sites, have their spins aligned in the upward direction. (6 Fe^{3+}), 2a (1 Fe^{3+}), and 2b (1 Fe^{3+}).

Table 2. Saturation magnetization (Ms), retentivity (Mr), coercivity (Hc), and magnetic moment (µB) of type hexaferrites for all compositions of $SrFe_{12-x}Sm_xO_{19}$ (x=0.00, 0.01, 0.05, and 0.09).

Sample Name	Sample symbol	Ms (emu/g)	Mr (emu/g)	Mr/Ms	Hc(Oe)	nβ(uβ)
$SrSm_{0.01}Fe_{11.99}O_{19}$	SF1	36.051	20.137	0.55	4873	7.80
$SrSm_{0.05}Fe_{11.95}O_{19}$	SF2	34.536	19.398	0.56	5154	7.43
$SrSm_{0.09}Fe_{11.91}O_{19}$	SF3	40.130	22.615	0.56	6135	8.57

The four downward spins and four upward spins cancel each other's effect, and due to the remaining 4 Fe^{3+} ions having an upward direction, the magnetic moment [32]. The values of retentivity (Mr) and saturation magnetization (Ms) are reduced due to the addition of a concentration of Sm^{3+} ions. The magnetic parameters were also calculated and reported in Table 2.

Magnetization is enhanced with A-site substitution. The Sm^{3+} ions have less magnetic moment than the Fe^{3+} ions. At B locale, the number of Fe^{3+} ions increased, so the magnetization of B sublattices increased, which results in enhanced magnetization in the Sm^{3+} substituted samples [33]. Results show that, as the samarium doping increases, the saturation magnetization and remanence increase, then decrease. The increase in the Ms value is noticed when $x>0.09$. The presence of Fe_2O_3 contributes to maintaining the electrical neutrality in the strontium hexaferrite. However, the increase of hyperfine fields in the 12K and 2b sites due to the superexchange interaction in Fe^{3+}- O - Fe^{3+}, leads to a higher magnetization in the lattice, and also affects the relative ionic radii of Sm^{3+} and (host) Fe^{3+}ions, which are (0.96Å) and (0.64Å) and cause a decrease of Ms value [34].

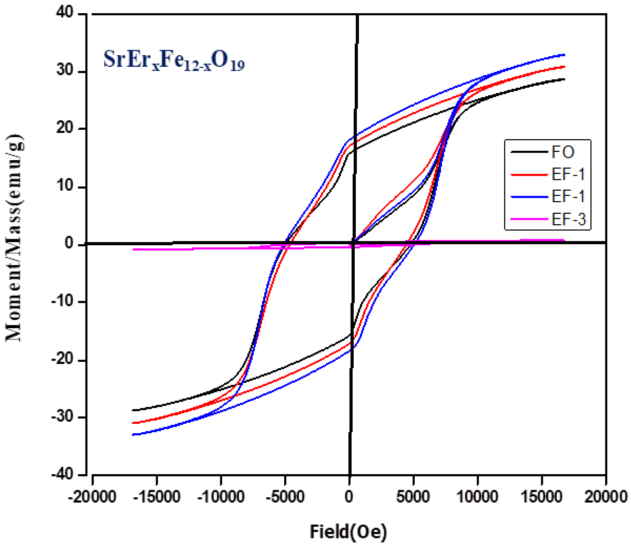

Figure 3. Hysteresis curves of $SrFe_{12-x}Sm_xO_{19}$ (x=0.00, 0.01, 0.05, and 0.09) nanoferrites.

The ionic radii of Sm^{3+} ions replaced the Fe^{3+} ions from 4f2 sites, and due to this, Hc decreases. Usually, in all hexagonal ferrites, one large divalent metal ion (Pb, Ba, or Sr) is mostly present, which causes a trivial interruption in the lattice because of the difference in size. In most cases, the c-axis is the favored orientation in all hexagonal ferrites. Hence, slack crystals line up within the c-axis when the direction of the applied field is perpendicular and haphazardly orient when the field direction is parallel [35,36].

3.6. Electrochemical methods.

3.6.1. Charge transfer behavior of modified electrode.

Preparation of a modified electrode by coating a layer of synthesized $SrFe_{12-x}Sm_xO_{19}$ in DMF on the surface of a glassy carbon electrode (GCE) to find out charge transfer behavior, and the modified electrode represented as $Fe_{12-x}Sm_xO_{19}$/GCE was used as a sensor for the redox reactions. Among the verified modified electrodes, $SrFe_{12-x}Sm_xO_{19}$/GCE was found to be more current-carrying. The cyclic voltametry (CV) instrument was standardized using $K_4[Fe(CN)_6]$ Figure 4. The bare GCE was taken first in the ferrocynide system for recording a cyclic voltammogram (CV). The electrochemical evaluation in 0.5 mM $K_4[Fe(CN)_6]$ solution at a scan rate of 50 mVs^{-1} between bare GCE and modified electrodes is represented in supplementary Figure S4. The bare GCE showed a current response of 4.322X10^{-5} µA, and the $SrFe_{12-x}Sm_xO_{19}$/GCE exhibits a more current response, i.e., 5.638X10^{-5}µA in the redox system, indicating that $SrFe_{12-x}Sm_xO_{19}$/GCE has good electro-conducting properties when compared to the bare GCE. The electrode acts as a bridge for electron transfer between the GCE surface and the buffer solution in a cyclic voltameter. The oxidation and reduction reaction of folic acid is shown below [37-39].

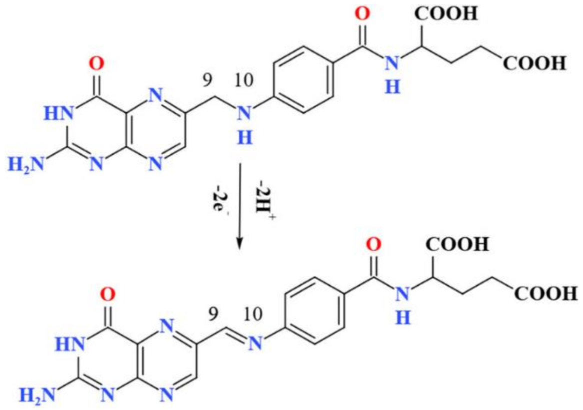

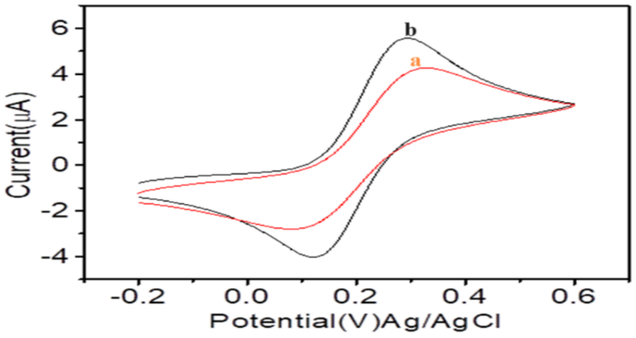

Figure 4. Cyclic voltammogram of 01 Mm KCl solution containing 0.5 mM $K_4[Fe(CN)_6]$ at the **(a)** bare GCE; **(b)** $SrFe_{12-x}Sm_xO_{19}$ /GCE, the scan rate:50 mVs^{-1}.

3.6.1.1. Electrochemical investigation of the modified electrode.

Electrochemical sensing of folic acid was studied in an electrolytic solution using a phosphate buffer solution of pH 7. The cyclic voltammogram of (i) bare GCE, (ii) $SrFe_{11.91}Sm_{0.09}O_{19}$ /GCE, with 100 µL concentration of folic acid at a scan rate of 50 mVs^{-1}. The $SrFe_{11.91}Sm_{0.09}O_{19}$/GCE electrode showed intensified peak current responses as compared to the bare glassy carbon electrode, and it is a good electrochemically active electrode, as represented in Figure 5 [40].

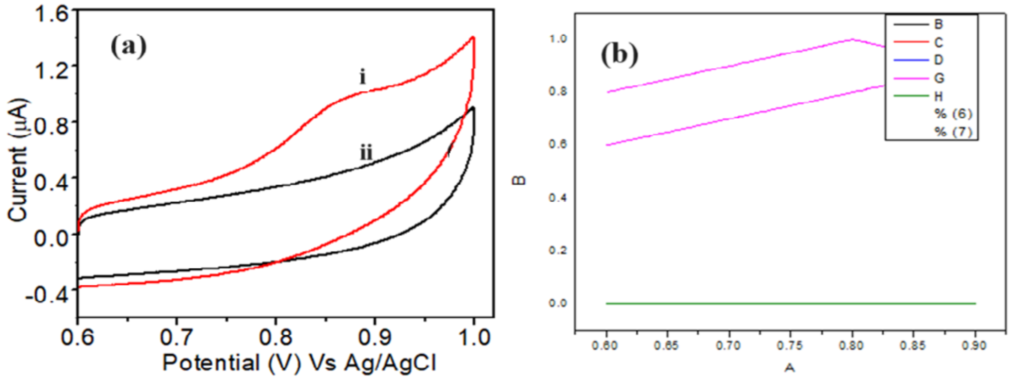

Figure 5. Electrochemical investigation of the **(a)** modified electrode (i) $SrFe_{11.91}Sm_{0.09}O_{19}$ /GCE, with 100 µL concentration of folic acid (ii) bare GCE: **(b)** inset: linear graph.

3.6.1.2. Effect of scan rate.

The scan rate was determined from 10 to 60 mVs^{-1} on sensor $SrFe_{11.91}Sm_{0.09}O_{19}$ /GCE. It was investigated that a linear relationship existed between peak current and scan rate, as presented in Figure 6(a). The plot of peak current vs scan rate, shown in Figure 6(b), indicated a diffusion-controlled process, with a correlation coefficient of 0.9954 µM, a sensitivity of 8.994 µM, and a linear regression equation of Ipa = 8.994 + 0.480 [41].

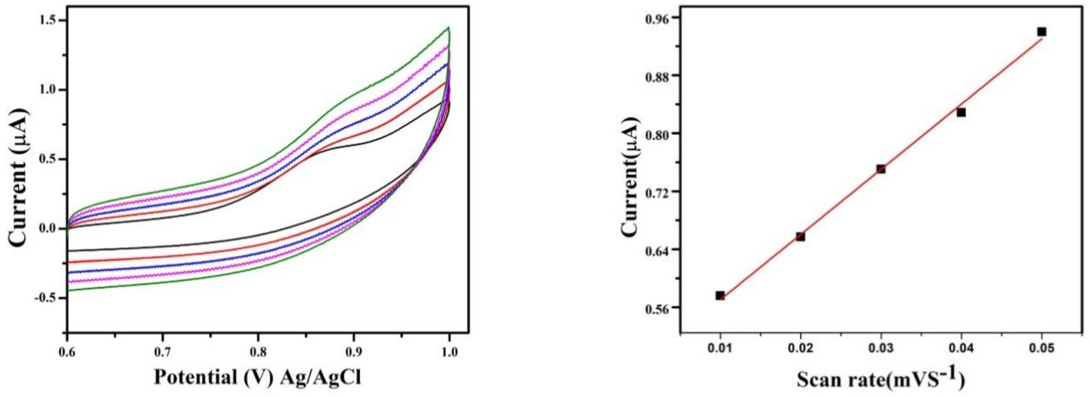

(a) (b)

Figure 6. (a) Cyclic voltammogram of folic acid at $SrFe_{11.91}Sm_{0.09}O_{19}$ /GCE scan rate ranging from (10-60mV). (b) Inset: plot of current (I) vs scan rate.

3.6.2. Detection of Folic acid in different concentrations.

The cyclic voltammetry(CV) of $SrFe_{11.91}Sm_{0.09}O_{19}$ /GCE in various concentrations of folic acid was recorded. In response to increasing folic acid concentration (Figure 7), the anodic peak current, IPa, also increased linearly while the peak potential shifted positively. This was confirmed when a peak potential of 0.8347 mV/s was noticed in the beginning, and the value of 0.910 mV/s shifted later. In addition, it was observed that the separation of peak potential increased with increasing peak current [42].

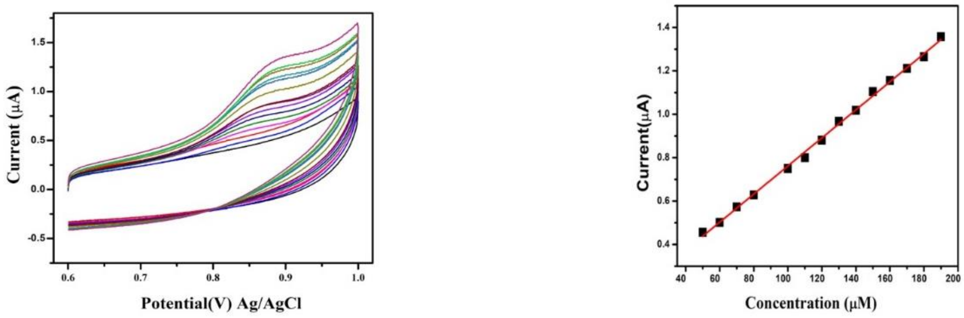

(a) **(b)**

Figure 7. (a) Using folic acid for different concentrations; **(b)** Linear graph obtained when folic acid used in different concentrations.

In addition to the linear regression equation y= 0.00649 -0.1145, a correlation value of R^2= 0.9978 was determined. Each point on the calibration graph corresponds to the 't' mean value obtained from independent measurements. The analytical profile detection limit is 16.667 µM, concentration range 50-190 µM, and sensitivity 0.00647.

3.6.3. Differential pulse voltammetry (DPV) studies of folic acid.

DPV was detected using folic acid and $SrFe_{11.91}Sm_{0.09}O_{19}$/GCE, which gives accurate results for the detection of folic acid in PBS with a pH of 7, and the results are collected in

Table 3. The reaction, which occurs as mentioned below, showed enhanced anodic peak current response when compared to bare GCE. The folic acid concentration ranges from 20 to 100 µM, and the peak current is enhanced at a fixed potential. The analytical profile of the modified electrode was a long linear range of 20 to 100 µM, a sensitivity of 0.0113 µM, and a LOD of 6.667 µM. Further, the results of the modified sensor were reproducible and have anti-leaching properties [43,44] as shown in Figure 8.

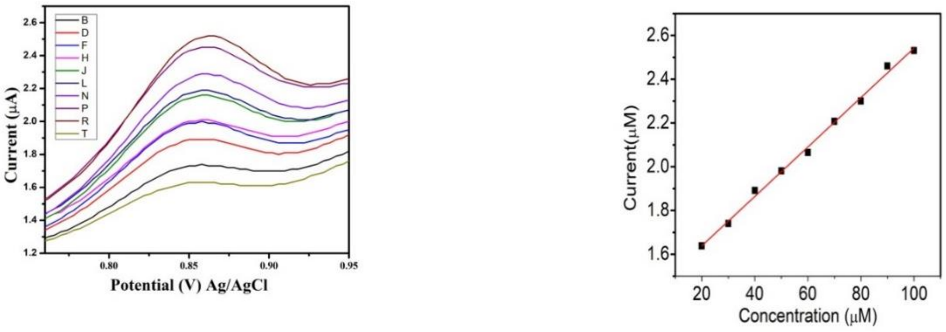

(a) **(b)**

Figure 8. (a) DPV of $SrFe11_{.91}Sm_{0.09}O_{19}$ /GCE at a concentration ranging from 20– 100 µM; **(b)** Calibration graph of current vs concentration linear graph.

Table 3. Comparison of the different actuators for folic acid determination.

Compound	Linear range (µM)	Technique	LOD (µM)	Sensitivity (µM)	Reference
CoTM-QOPc /CNP/GCE	0.2-200 0.2-225	CV DPV	0.06 0.06	2.298 1.031	[15]
CoL/MNSs/CPE	0.2-30.0	SWV	0.015	-	[39]
Co_3O_4/RGO	1-380	CV	0.14	29.5	[40]
CRS/BN RGO/GCE	0.001- 1290	DPV	0.0159	1.5309	[41]
$SrFe_{11.91}Sm_{0.09}O_{19}$	50-190 20-100	CV DPV	16.66 6.667	0.00647 0.0113	**Present work**

4. Conclusions

In the present investigation, samarium-doped strontium M-type hexagonal ferrites $SrFe_{12-x}Sm_xO_{19}$ (x=0.00, 0.01, 0.05, and 0.09) nanoparticles have been synthesized through the auto-combustion method. XRD investigation revealed the existence of a hexagonal structure with the absence of Sm_3O_3 as a separate phase. The scanning electron microscope indicated that the platelets are like grains and have a well-defined, irregular shape. FTIR analysis for pure and doped strontium ferrite samples indicated that Fe-O stretching modes, which appear around 587 cm^{-1}, and also revealed that the introduction of Sm^{3+} ions could reduce crystalline size. Hysteresis curves from VSM analysis indicate that at room temperature, it exhibited ferromagnetic behavior for x=0.01 to 0.09. Coercivity more than 1.3kOe and investigated the hard magnetic nature of these samples. Results show that as doping increases, the Ms and Mr also increase continuously. The modified electrode was prepared to evaluate the electrocatalytic activity of the redox system, which could also be used to detect biologically important molecules such as folic acid with a sensitivity of 0.0113 µM by cyclic voltammetry and differential pulse voltammetry.

Author Contribution

Writing – original draft preparation – A.T.; Writing – review & editing – A.T., P.C., G.K.; Resources – P.C.; Data curation – P.C.; Formal analysis – P.C.; Supervision – G.K. All authors have read and agreed to the published version of the manuscript.

Institutional Review Board Statement

Not applicable.

Informed Consent Statement

Not applicable.

Data Availability Statement

Data supporting the findings of this study are available upon reasonable request from the corresponding author.

Funding

This research received no external funding.

Acknowledgments

The authors are grateful to the Department of Chemistry, Sahyadri Science College, Shivamogga, for providing experimental facilities, and one of the authors is thankful to VGST-K-Fist-L1, Govt. of Karnataka, for providing instrumentation facilities like FTIR, UV-Visible, and CV. The authors also extend their thanks to USIC, University of Guwahati, Assam, India, for providing the VSM spectral data.

Conflicts of Interest

The authors declare no conflict of interest.

References

1. Baba, B.D.; Suresh, K.N.; Chandra, B.N.K. Structural, electrical, and magnetic properties of nano $Sr_{1-X}La_XFe_{12}O_{19}$ (X = 0.2–0.8). *Sci. Rep*. **2022**, *12*, 12723, https://doi.org/10.1038/s41598-022-15250-2.
2. Jiang, Z.; Han, X.; Zhao, C.; Wang, S.; Tang, X. Recent Advance in Biological Responsive Nanomaterials for Biosensing and Molecular Imaging Application. *Int. J. Mol. Sci.* **2022**, *23*, 1923, https://doi.org/10.3390/ijms23031923.
3. Rozita, S.; Ahmad, G. The effect of the annealing temperature on the microstructural, magnetic, and spin-dynamical properties of Mn–Mg–Cu–Zn ferrites. *Phys. B Condens. Matter.* **2022**, *624*, 413442, https://doi.org/10.1016/j.physb.2021.413442.
4. Mehwish, S.; Safia, A.; Yasin, R.; Zeeshan, M.; Anam, M.; Rabia, K.; Tafruj, I. Samarium substituted M-type Sr hexaferrites: The structural, magnetic and electrochemical properties for supercapacitor applications. *Ceram. Int.* **2024**, *50*, 16747-16764, https://doi.org/10.1016/j.ceramint.2024.01.224.
5. Ishfaq, A.P.; Anand, S.; Syyed, A.A. Study of microstructural, ferroelectric and magnetic properties of cerium substituted magnesium ferrite and its potential application as hydroelectric cell. *Ceram. Int*. **2023**, *49*, 6946-6957, https://doi.org/10.1016/j.ceramint.2022.10.223.
6. Xuelu, X.; Yue, D.; Qingwen. H.N.S.; Chunwei, Z. Electrochemical Hydrogen Storage Materials: State-of-the-Art and Future Perspectives. *Energy Fuels* **2024**, *38*, 7579-7613, https://doi.org/10.1021/acs.energyfuels.3c05138.
7. Ashutosh, T.; Pawan, G.; Amit, K. M. Outlooks of Nanosensors in Medical and Smart Devices, Agricultural and Food Technology. *L. Appl. NanoBioSci.* **2024**, *13*, 142, https://doi.org/10.33263/LIANBS133.128.
8. Mohammed, L.R.; Salina, R.; Bristy, B.; Mohammed, F.A.; Moksodur, R.; Nahid, S. Investigation of structural, morphological and magnetic properties of nanostructured strontium hexaferrite through co-precipitation technique: Impacts of annealing temperature and Fe/Sr ratio. *Heliyon* **2023**, *9*, e14532, https://doi.org/10.1016/j.heliyon.2023.e14532.

9. Mathin, S.A.; Raju, M.D.; Reddy, D.R.S. Function of ZnO Nanoparticles in the Remediation of the Toxic Metal, Seed Germination, and Seedling Growth of the Plant, Synthesized by Stem Extracts of *Anthophalus cadamba*. *Lett. Appl. BioNanoSci.* **2023**, *12*, 23, https://doi.org/10.33263/LIANBS121.023.
10. Joshi, C.S.; Srivastava, R.C.; Joshi, A. Structural, magnetic and dielectric properties of cerium-doped manganese–cobalt ferrite nanoparticles. *J. Mater. Sci. Technol.* **2024**, *40*, 953-968, https://doi.org/10.1177/0267083624123419.
11. El Shater, R.E.; El-Desoky, H.S.; Meaz, T.M. Electrochemical investigation of Ag mixed Cd–Cu nanoferrite mixed reduced graphene oxide as improved platform for supercapacitor application. *J. Mater. Sci. Mater. Electron.* **2023**, *34*, 842, https://doi.org/10.1007/s10854-023-10023-7.
12. Shikhil, S.W.; Deoram, V.N.; Amit, V.G. Investigating impact of Ni-Cd substitution on structural magnetic and optical properties of nanosize Al ferrites. *Heliyon* **2024**, *10*, e39734, https://doi.org/10.1016/j.heliyon.2024.e39734.
13. Ramadan, R. Zinc-doped hexaferrite exhibits altered physical properties in the presence of both Dy and Zn ions. *J. Mater. Sci. Mater. Electron.* **2024**, *35*, 1402, https://doi.org/10.1007/s10854-024-13098-y.
14. Krishnapriya, T.K.; Prasanth, S.; Deepti, A.; Baby Chakrapani, P.S.; Asha, A.S.; Jayaraj, M.K. Ultrafast detection of folic acid in nanomolar levels and cancer cell imaging using hydrothermally synthesized carbon dots. *J. Microchemical.* **2023**, *188*, 108470, https://doi.org/10.1016/j.microc.2023.108470.
15. Dipan, B.; Shreya, N.; Debangana, D.; Runu, B.R. Electrochemical detection of folic acid in food extracts using molecularly imprinted polyacrylonitrile imbued graphite electrode. *Anal. Chim. Acta.* **2024**, *1325*, 343120, https://doi.org/10.1016/j.aca.2024.343120.
16. Lakshmikantha, J.; Krishnamurthy. G.; Nagabhushan, B. M.; Naveen, C. S.; Melagiriyappa, E. Effect of Ce^{3+} Substitution on Sr^{2+}; Structural and Magnetic Properties of Nanocrystalline $SrFe_{12}O_{19}$ Hexaferrites Prepared by Self-Propagation Method Using Mixed Fuels. *J. Supercond. Nov. Magn*. **2022**, *35*, 2485-2492, https://doi.org/10.1007/s10948-022-06223-7.
17. Lakshmikantha, J.; Krishnamurthy, G.; Nagabhushan, B. M. Dielectric properties and magnetic behavior of Gd^{3+} substituted M-type $SrFe_{12}O_{19}$ nanoferrites by auto combustion method using urea and citric acid mixtures as a dual fuel. *J. Solid State Chem*. **2022**, *315*, 123465, https://doi.org/10.1016/j.jssc.2022.123465.
18. Gao, C.; Shi, J.W.; Fan, W.Z.Y.; Wang, B.R.; He, Y.C. Fast S.C.R. reaction over Sm modified MnOx-TiO_2 for promoting reduction of NOx with NH_3. *Appl. Catal. A.* **2018**, *564*, https://doi.org/10.1016/j.apcata.2018.07.017.
19. Yafet, C.; Kittle, Y. Anti ferromagnetic arrangements in ferrites. *J. Phys. Rev*. **2018**, *87*, 290-294, https://doi.org/10.1103/PhysRev.87.290.
20. Aamir, S.M.; Raqiqa, T.R.; Imdadullah, Q.; Saeed, A.B.M.; Sana, B.; Ghulam A.A.; Muhammad, A.K. Impact of samarium on structural and dielectric properties of U-type hexaferrites synthesized by a sol-gel auto combustion route: Analysis of XPS, Raman and FTIR spectra. *Ceram. Int.* **2024**, *50*, 11639-11649, https://doi.org/10.1016/j.ceramint.2024.01.066.
21. Hemalatha, K.A.; Arulmozhi, R.; Chandunika, R.; Niroj, S.; Parthipan, G.; Muralidharan, R. Cytotoxic effect of functionalized super paramagnetic samarium doped iron oxide nanoparticles for hyperthermia application. *Mater. Res. Innov.* **2022**, *48*, 24485-24495, https://doi.org/10.1016/j.ceramint.2022.05.078.
22. Thippeswamy, A.; Manjunatha, M.N.; Chavan, P.; Krishnamurthy, G. Synthesis, Structural, Magnetic, And Electrochemical Properties of Er-Ni Doped Strontium Nanoferrites. *Anal. Bioanal. Electrochem.* **2024**, *16*, 1026-1045, https://doi.org/10.22034/abec.2024.718628.
23. Shaila, G.S.; Manjanna, J.; Mohan, K. A simple and efficient electrochemical sensor for folic acid determination on $Ti(OH)_4$ modified carbon paste electrode. *Inorg. Chem. Commun*. **2024**, *168*, 112912, https://doi.org/10.1016/j.inoche.2024.112912.
24. Lokesh, K.S.; Jilani, B.S.; Malathesh, P.; Venugopal, K.R.; Mounesh. Simultaneous and sensitive detection of ascorbic acid in presence of dopamine using MWCNTs-decorated cobalt (II) phthalocyanine modified G C. *J. Microchem*. **2019**, *5*, 755-763, https://doi.org/10.1016/j.microc.2019.03.090.
25. Mounesh; Malathesh, P.; Kumara, P.; Jilan, N.Y.; Mruthyunjayachari, C.D.; Venugopal, K.R. Synthesis and characterization of tetra-ganciclovir cobalt (II) phthalocyanine for electroanalytical applications. *Heliyon* **2019**, *5*, e01946, https://doi.org/10.1016/j.heliyon.2019.e01946.
26. Badreddine, K.; Kazah, R.M.; Awad, R. Structural, Morphological, Optical, and Room Temperature Magnetic Characterization on Pure and Sm-Doped ZnO Nanoparticles. *J. Nanomater.* **2018**, *2018*, 7096195, https://doi.org/10.1155/2018/7096195.

27. Silva-Soares, P. da.; Costa-Catique, L. da.; Guerrero, F.; Mariño-Castellanos, P.A.; Govea-Alcaide, E.; Romaguera-Barcelay,Y.; Rodrigues. A.R.; Padron-Hernandez, E.; Pena-Garcia, R. Investigation of structural and magnetic properties of Al substituted $Ba_{0.9}La_{0.1}Fe_{12-x}Al_xO_{19}$ hexaferrites prepared by solid-state reaction method. *J. Magn. Magn. Mater*. **2022**, *547*, 168958, https://doi.org/10.1016/j.jmmm.2021.168958.
28. Yasmin, N.; Mirza, M.; Safdar, M.; Zahid, M.; Ahmad, M.; Awan, M.S.; Altaf, M. Influence of Samarium Substitution on the Structural and Magnetic Properties of M-type Hexagonal Ferrites. *Magn. Magn. Mater*. **2017**, *17*, 31928-5, http://dx.doi.org/10.1016/j.jmmm.2017.09.005.
29. Mousavi, G.S.E.; Shobegar, E.M.; Shoushtari, M. Z.; Effects of Sintering Temperature on Structural, Morphological and Magnetic Properties of Strontium Ferrite Nanoparticles. *J. Supercond. Nov. Magn*. **2018**, *32*, 1067-1076, https://doi.org/10.1007/s10948-018-4799-0.
30. Hemalatha, K.; Alamelumangai, R.; Arulmozhi, P.G.; Rajara, M. Magnetic and X-ray photo electron spectroscopic analysis of samarium doped iron oxide nanoparticles. *Matter. Res. Innov*. **2020**, *25*, 372-379, https://doi.org/10.1080/14328917.2020.1827815.
31. Dung, N. K.; Huyen, N.T.L. Significantly improving magnetic properties of Sr-La-Co hexagonal ferrite. *J. Math. Phys*. **2009**, *25*, 199–205.
32. Sankaranarayanan, V.K.; Khan, D.C. Mechanism of the formation of nanoscale M-type barium hexaferrite in the citrate precursor method. *J. Magn. Magn. Mater. **2020** 153*, 337-346, https://doi.org/10.1016/j.matpr.2020.12.011.
33. Skomski, R.; Topal, U.; Husnu, Ozkan.; Huseyin, S. Synthesis and characterization of nanocrystalline $BaFe_{12}O_{19}$ obtained at 850°C by using ammoniumnitrate melt. *J. Magn. Magn. Mater*. **2004**, *284*, 416-422, https://doi.org/10.1016/j.jmmm.2004.07.009.
34. Muhammad, A.; Muhammad, A.K.; Ghulam, A. A.; Khalid, M.; Muhammad I. A.; Investigation of crystal structure, electrical and dielectric response of Zr^{4+} -Co^{2+} substituted Ba–Sr–Ni Y-type hexagonal ferrites synthesized by sol-gel route. *Ceram. Int.* **2023**, 49, 4141-4152, https://doi.org/10.1016/j.ceramint.2022.09.296.
35. Liu, X.; Zhong.; Yang, W.S.; Yu, Z.; Gu, B.Y. Influences of La^{3+} substitution on the structure and magnetic properties of M-type strontium ferrites. *J. Magn. Magn. Mater.* **2002**, *238*, 207-214, https://doi.org/10.1016/S0304-8853(01)00914-3.
36. Dlugosz, O.; Szostak, K.; Krupinski, M.; Banach, M.; Synthesis of Fe_3O_4/ZnO nanoparticles and their application for the photodegradation of anionic and cationic dyes. *Int. J. Environ. Sci. Technol.* **2021**, *18*, 561–574, https://doi.org/10.1007/s13762-020-02852-4.
37. Kumar, M.; Kumaraswamy, E.; Venugopal, K.R.; Zhao, W.; Chetana, S.; Gowravkumar. V. ZnO/functionalized MWCNT and Ag/functionalized MWCNT modified carbon paste electrodes for the determination of dopamine, paracetamol and folic acid. *J. Electr. Anal. Chem*. **2019**, *835*, 96-105, https://doi.org/10.1016/j.jelechem.2019.01.019.
38. Jilani, B.S.; Mounesh.; Malathesh, P.; Mruthyunjayachari, C.D.; Venugopal, K.R.; Cobalt (II) tetra methyl quinoline oxy bridged phthalocyanine carbon nano particles modified glassy carbon electrode for sensing nitrite: A voltammetric study. *Mater. Chem. Phys*, **2020**, *239*, 121920, https://doi.org/10.1016/j.matchemphys.2019.121920.
39. Mozhgan, P.; Zahra, A.; Saeid, K.; A sensitive electrochemical sensor for rapid and selective determination of nitrite ion in water samples using modified carbon paste electrode with a newly synthesized cobalt(II)-Schiff base complex and magnetite nanospheres. *Sens. Actuators B Chem.* **2015**, *220*, 1131–1138, https://doi.org/10.1016/j.snb.2015.06.096.
40. Mahboobeh Amini, Ahmad Gholizadeh, Shape control and associated magnetic and dielectric properties of $MFe_{12}O_{19}$ (M = Ba, Pb, Sr) hexaferrites, J. Phys. Chem. Solids. 2020, 147, 109660, https://doi.org/10.1016/j.jpcs.2020.109660
41. Vinitha, M.; Ming, S.; Chen, K.; M.; Alagan, J.; Tharini, J.; Rasu, R. Electrochemical sensor based on cobalt ruthenium sulfide nanoparticles embedded on boron nitrogen co- doped reduced graphene oxide for the determination of nitrite. *Colloid. Surf. A Physicochem. Eng. Asp.* **2022**, *637*, 128271, https://doi.org/10.1016/j.colsurfa.2022.128271.
42. Wang, Y.N.; Wu, Y.Y.; Yang, X.Q.; Li, L.H.; Qi, B. Optimization of Nitrite Reductase Production Conditions in Lactobacillus plantarum from Salted Fish. *Adv. Mater. Res*. **2013**, *781-784*, 1595-1598, https://doi.org/10.4028/www.scientific.net/AMR.781-784.1595.

43. Vasantakumaranaik, N.; Krishnamurhty, G.; Malathesh, P.; Venugopal, N.; Nagarajanaik, N. Synthesis Spectral Characterisation of Novel Azo–Dye 4 ((E)-(2Hydroxy-3- Methoxy-5-((E)-Thiazol-2 ldiazenyl)Benzyliden -1,5-Dimethyl-2-Phenyl 1H-Pyrazol-3(2H)- One and its Transition Metal Complexes; Differential Pulse Voltammetric. Detection of Nitrite and its Biological Activities. *J. Biointerface Res. Appl. Chem*. **2023**, *13*, 531, https://doi.org/10.33263/BRIAC136.531.
44. Jithendra, K.S.; Krishnamurthy, G.; Kumarnaik, N.S.N.; Praveen, T.M. Sustainable synthesis of magnetically separable $SiO_2/Co@Fe_2O_4$ nanocomposite and its catalytic applications for the benzimidazole synthesis. *Mater. Res. Innov.* **2017**, *451*, 808–821, https://doi.org/10.1016/j.jmmm.2017.10.125.

Publisher's Note & Disclaimer

Supplementary materials

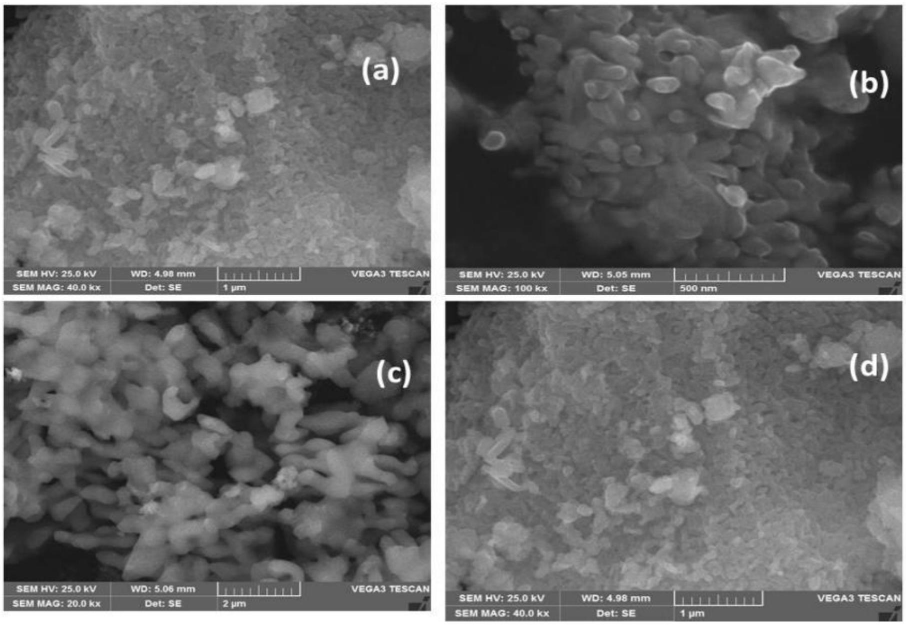

Figure S1. SEM micrographs of M-type hexaferrites $SrFe_{12-x}Sm_xO_{19}$ for all compositions (a) x=0.00, (b) x=0.01, (c) x=0.05 and (d) x=0.09.

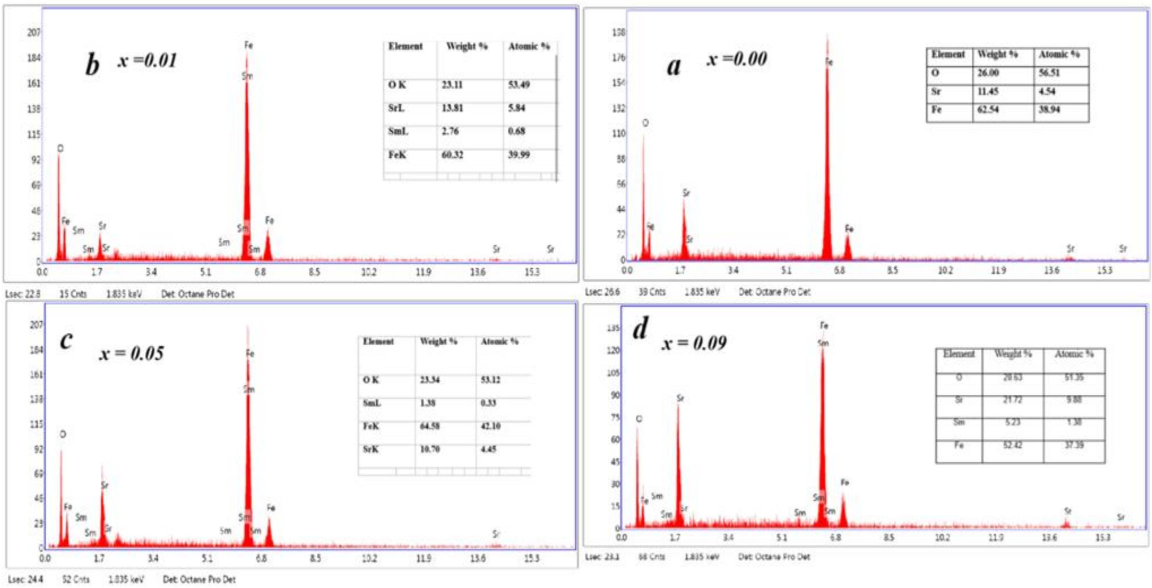

Element	Weight %	Atomic %
O K	23.11	53.49
SrL	13.81	5.84
SmL	2.76	0.68
FeK	60.32	39.99

Element	Weight %	Atomic %
O	26.00	56.51
Sr	11.45	4.54
Fe	62.54	38.94

Element	Weight %	Atomic %
O K	23.34	53.12
SmL	1.38	0.33
FeK	64.58	42.10
SrK	10.70	4.45

Element	Weight %	Atomic %
O	20.63	51.35
Sr	21.72	9.88
Sm	5.23	1.38
Fe	52.42	37.39

Figure S2. Elemental mapping and EDX spectrum of $SrFe_{12-x}Sm_xO_{19}$ nanoparticles with a temperature of 900 °C, (a) x=0.00, (b) x=0.01, (c) x=0.05 and d) x=0.09.

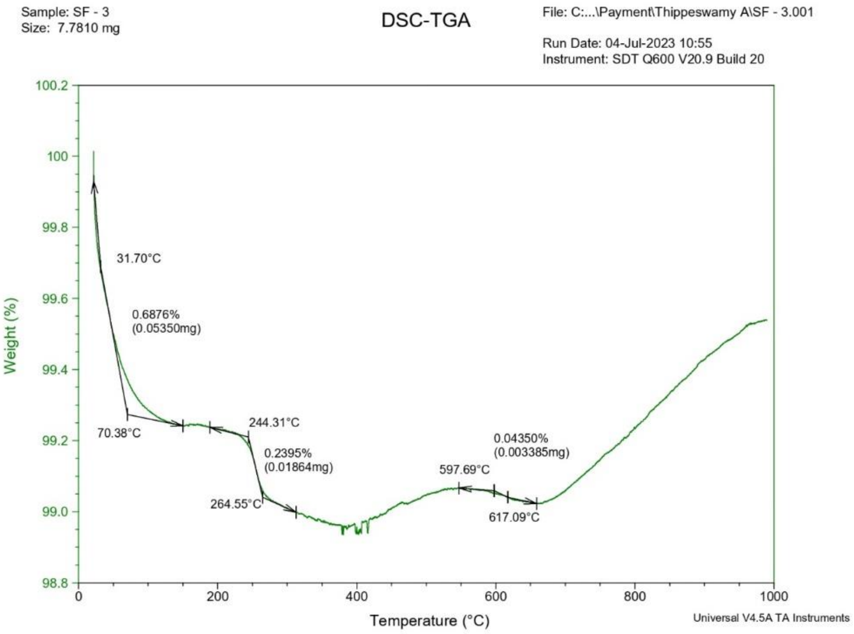

Figure S3. TGA-DSC curves of $SrFe_{11.91}Sm_{0.09}O_{19}$ nanoferrite.

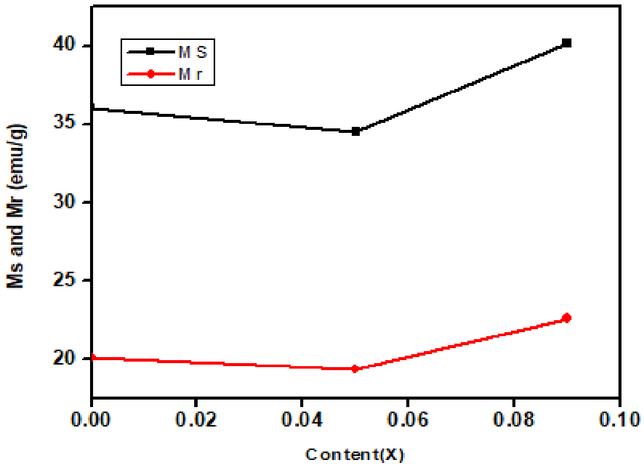

Figure S4. Variation of Ms and Mr of $SrFe_{12-x}Sm_xO_{19}$ (x=0.00<x<0.09) as a function of Sm^{3+} contents.